Computation and Evaluation of Medial Surfaces for Shape Representation of Abdominal Organs

Sergio Vera[1,2], Debora Gil[1], Agnès Borràs[1], Xavi Sánchez[1], Frederic Pérez[2], Marius G. Linguraru[3], and Miguel A. González Ballester[2]

[1] Computer Vision Center, Computer Science Dept., Universitat Autònoma de Barcelona, Spain
[2] Alma IT Systems, Barcelona, Spain
[3] Radiology and Imaging Sciences Dept., Clinical Center, National Institutes of Health, Bethesda, USA
sergio.vera.h@gmail.com

Abstract. Medial representations are powerful tools for describing and parameterizing the volumetric shape of anatomical structures. Existing methods show excellent results when applied to 2D objects, but their quality drops across dimensions. This paper contributes to the computation of medial manifolds in two aspects. First, we provide a standard scheme for the computation of medial manifolds that avoid degenerated medial axis segments; second, we introduce an energy based method which performs independently of the dimension. We evaluate quantitatively the performance of our method with respect to existing approaches, by applying them to synthetic shapes of known medial geometry. Finally, we show results on shape representation of multiple abdominal organs, exploring the use of medial manifolds for the representation of multi-organ relations.

Keywords: medial manifolds, abdomen.

1 Introduction

Abdominal diagnosis relies on the comprehensive analysis of groups of organs [10]. Besides the organ appearance and size, the shapes of the organs can be indicators of disorders. Abdominal organs follow global shape constraints, which have proved exceptionally useful to guide segmentation algorithms, for example for the liver [8]. Although local shape differences are key to diagnosis, they are difficult to model without an adequate shape representation [14].

Medial manifolds of organs have proved robust and accurate to study group differences in the brain [4,17]. In the abdomen, shape-based modeling could reveal biomarkers for diagnosis by identifying unusual anatomy and its relation to neighboring organs. Additionally, organ locations, generally defined by centroids [19], and more recently by pose [11], can be more comprehensively characterized by medial manifolds, more intuitive and easily interpretable representations of complex organs.

In order to provide accurate meshes of anatomical geometry, the extraction of medial manifolds should satisfy three main conditions [13]: *homotopy* (mantain the same topology of the original shape), *thinness* (the resulting medial shape should be one pixel wide, taking into account the specific choice of connectivity), and *medialness* (the medial structure should lie as close as possible to the center of the original object). Most

H. Yoshida et al. (Eds.): Abdominal Imaging 2011, LNCS 7029, pp. 223–230, 2012.

methods for medial surface computation are based on morphological thinning operations on binary segmentations. Such methods require the definition of a neighborhood set and conditions for the removal of *simple voxels*, i.e. voxels that can be removed without changing the topology of the object. These definitions are trivial in 2D, but their complexity increases exponentially with the dimension of the embedding space [9]. Further, simplicity tests alone only produce (1D) medial axis so additional tests are needed to know if a voxel lies in a surface and thus cannot be deleted even if it is simple [13]. Moreover, surface tests might introduce medial axis segments in the medial surface, which is against the mathematical definition of manifold and that may require further pruning [13,1].

Alternative methods rely on an energy map to ensure medialness on the manifold. Often, this energy image is the distance map of the object [13] or another energy derived from it, like the average outward flux [16,4], level set [15,18] or ridges of the distance map [6]. However, to obtain a manifold from the energy image, most methods rely on morphological thinning, in a two step process [4,13,16], thus inheriting the weak points of morphological methods.

The contribution of this paper is a two step method for medial surface computation based on the ridges of the distance map. Firstly, as energy image we propose the ridges of the distance map, based on a normalized ridge operator. Secondly, our binarization step is free of topology rules, as it is based on Non-Maxima Suppression (NMS) [5]. Given that, regardless of the space dimension, NMS only requires 1 direction to be defined, our method scales well with dimension. Quantitative evaluation of our method in comparison with existing approaches is shown on synthetic shapes of known medial geometry. Finally, results are shown on sets of segmented livers obtained from [8], as well as multi-organ datasets [14].

2 Extracting Anatomical Medial Surfaces

The computation of medial manifolds from a segmented volume may be split into two main steps: computation of a medial map from the original volume and binarization of such map. Medial maps should achieve a discriminant value on the shape central voxels. Meanwhile, the binarization step should ensure that the resulting medial structures fulfill the three conditions: medialness, thinness and homotopy.

Distance transforms are the basis for obtaining medial manifolds in any dimension. The distance map is generated by computing the Euclidean distance transform of the binary mask representing the volumetric shape. By definition, the maximum values of the distance map are located at the center of the shape at voxels corresponding to the medial structure. It follows that the medial surface could be extracted from the raw distance map by an iterative thinning process [13]. Two alternative binarizations that scale well with dimension are thresholding and NMS. Thresholding keeps pixels with medial map energy above a given value. Therefore, it requires that the medial map is constant along the medial surface. Non-Maxima Suppression keeps only those pixels attaining a local maximum of the medial map in a given direction. Unless the medial map maxima are flat, NMS also produces one pixel-wide surfaces.

Further examination of the distance map shows that its central maximal voxels are connected and constitute a ridge surface of the distance map. We propose using a normalized ridge map with NMS-based binarization for computing medial surfaces.

2.1 Normalized Medial Map

Ridges/valleys in a digital N-Dimensional image are defined as the set of points that are extrema (minima for ridges and maxima for valleys) in the direction of greatest magnitude of the second order directional derivative [7]. From the available operators for ridge detection, we chose the creaseness measure described in [12] because it provides (normalized) values in the range $[-N, N]$. The ridgeness operator is computed by the structure tensor of the distance map as follows.

Let D denote the distance map to the shape and let its gradient, ∇D, be computed by convolution with partial derivatives of a Gaussian kernel:

$$\nabla D = (\partial_x D_\sigma, \partial_y D_\sigma, \partial_z D_\sigma) = (\partial_x g_\sigma * D, \partial_y g_\sigma * D, \partial_z g_\sigma * D)$$

being g_σ a Gaussian kernel of variance σ and ∂_x, ∂_y and ∂_z partial derivative operators. The structure tensor or second order matrix [2] is given by averaging the projection matrices onto the distance map gradient:

$$ST_{\rho,\sigma}(D) = \begin{pmatrix} g_\rho * \partial_x D_\sigma^2 & g_\rho * \partial_x D_\sigma \partial_y D_\sigma & g_\rho * \partial_x D_\sigma \partial_z D_\sigma \\ g_\rho * \partial_x D_\sigma \partial_y D_\sigma & g_\rho * \partial_y D_\sigma^2 & g_\rho * \partial_y D_\sigma \partial_z D_\sigma \\ g_\rho * \partial_x D_\sigma \partial_z D_\sigma & g_\rho * \partial_y D_\sigma \partial_z D_\sigma & g_\rho * \partial_z D_\sigma^2 \end{pmatrix} \quad (1)$$

for g_ρ a Gaussian kernel of variance ρ. Let V be the eigenvector of principal eigenvalue of $ST_{\rho,\sigma}(D)$ and consider its reorientation along the distance gradient, $\tilde{V} = (P, Q, R)$, given as:

$$\tilde{V} = \text{sign}(< \tilde{V} \cdot \nabla D >) \cdot \tilde{V}$$

for $< \cdot >$ the scalar product. The ridgeness measure [12] is given by the divergence:

$$\mathcal{R} := \text{div}(\tilde{V}) = \partial_x P + \partial_y Q + \partial_z R \quad (2)$$

The above operator assigns positive values to ridge pixels and negative values to valley ones. The more positive the value is, the stronger the ridge patterns are. A main advantage over other operators (such as second order oriented Gaussian derivatives) is that $\mathcal{R} \in [-N, N]$ for N the dimension of the volume. In this way, it is possible to set a threshold, τ, common to any volume for detecting significant ridges and, thus, points highly likely to belong to the medial surface.

2.2 Non-maxima Suppression Binarization

We use NMS to obtain the voxels with higher ridgeness value and obtain a thin, one pixel wide medial surface. NMS consists in checking the two neighbors of a pixel in a specific direction, V, and delete pixels if their value is not the maximum one:

$$NMS(x,y,z) = \begin{cases} \mathcal{R}(x,y,z) & \text{if } \mathcal{R}(x,y,z) > \max(\mathcal{R}_{V+}(x,y,z),\ \mathcal{R}_{V-}(x,y,z)) \\ 0 & \text{otherwise} \end{cases}$$

for $\mathcal{R}_{V+} = \mathcal{R}(x+V_x, y+V_y, z+V_z)$ and $\mathcal{R}_{V-} = \mathcal{R}(x-V_x, y-V_y, z-V_z)$.

A main requirement is identifying the local-maxima direction from the medial map derivatives. The search direction for local maxima is obtained from the structure tensor of the ridge map, $ST_{\rho,\sigma}(\mathcal{R})$. The eigenvector of greatest eigenvalue of the structure tensor indicates the direction of highest variation of the ridge image. In order to overcome small glitches due to discretization of the direction, NMS is computed using interpolation along the search direction.

One drawback of the ridge operator is that anywhere the structure tensor does not have a clear predominant direction, the creaseness response decreases. This may happen at points where two medial manifolds join and can introduce holes on the medial surface that violate the homotopy principle. Such holes are exclusively localized at self-intersections, and are removed by means of a closing operator.

3 Validation Experiments

As multiple algorithms generate different surfaces, we are interested in finding a way to evaluate the quality of the generated manifold as a tool to recover the original shape. We propose a benchmark for medial surface quality evaluation that starts from known medial surfaces, that we consider as ground truth, and generates objects from them. The medial surface obtained from the newly created object is then compared against the ground truth surface. We have applied our NMS using $\sigma = 0.5$, $\rho = 1$ for both $ST_{\rho,\sigma}(D)$ and $ST_{\rho,\sigma}(\mathcal{R})$. In order to compare to morphological methods, we also applied an ordered thinning using a 6-connected neighborhood (labeled Thin6C) described in [3], a 26-connected neighborhood (labeled Thin26C) described in [13] and a pruning of the 26-connected neighborhood (labeled Thin26CP).

The quality of medial surfaces has been assessed by comparing them to ground truth surfaces in terms of surface distance [8]. The distance of a voxel y to a surface X is given by: $d_X(y) = \min_{x \in X} \|y - x\|$, for $\|\cdot\|$ the Euclidean norm. If we denote by X the reference surface and Y the computed one, the scores considered are:

1. *Standard Surface Distances*:

$$AvD = \frac{1}{|Y|}\left(\sum_{y \in Y} d_X(y)\right) \qquad MxD = \max_{y \in Y}(d_X(y))$$

2. *Symmetric Surface Distances*:

$$AvSD = \frac{1}{|X|+|Y|}\left(\sum_{x \in X} d_Y(x) + \sum_{y \in Y} d_X(y)\right)$$

$$MxSD = \max\left(\max_{x \in X}(d_Y(x)), \max_{y \in Y}(d_X(y))\right)$$

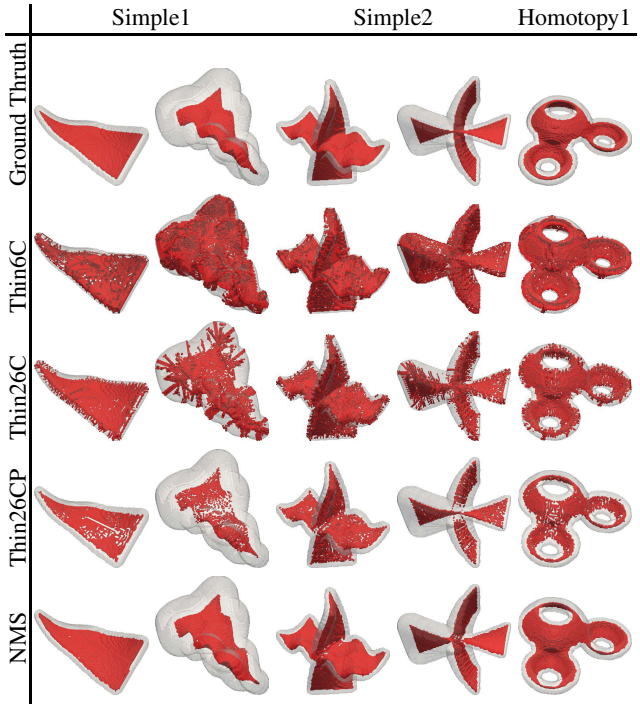

Fig. 1. Synthetic Volume examples. Each row corresponds to a compared method, while columns exemplify the different objects families tested: one and two foil surfaces, with constant (1st and 3rd columns) or variable distance (2nd and 4th columns), and with holes (last column).

Standard distances measure deviation from medialness, while differences between standard and symmetric distances indicate homotopy artifacts. Thinness has been visually assessed.

The ground truth medial surfaces cover 3 types: non-intersecting trivial homotopy (denoted Simple1), intersecting trivial homotopy (denoted Simple2) and non-trivial (homeomorphic to the circle) homotopy group (denoted Homotopy1). Thirty volumes having the synthetic surfaces as medial manifolds have been generated by thresholding the distance map to the synthetic surface. We have considered constant (denoted UnifDist) and varying (denoted VarDist) thresholds.

Figure 1 shows an example of the synthetic volumes in the first row and results in the remaining rows. The shape of surfaces produced using morphological thinning strongly depends on the connectivity rule used. In the absence of pruning, surfaces, in addition, have extra medial axes attached. On the contrary, NMS medial surfaces have a well defined shape matching the original synthetic surface.

Table 1 reports error ranges for the four methods and the different types of synthetic volumes. For all methods, there are not significant differences between standard

and symmetric distances for a given volume. This indicates a good preservation of homotopy. Thinning without pruning has significant geometric artifacts (maximum distances increase) and might drop its performance for variable distance volumes due to a different ordering for pixel removal. The performance of NMS presents high stability across volume geometries and produces accurate surfaces matching synthetic shapes. These results show that our approach has better reconstruction power.

Table 1. Error ranges for the Synthetic Volumes

		Simple1		**Simple2**		**Homotopy1**
		UnifDist	VarDist	UnifDist	VarDist	
NMS	**AvD**	0.218 ± 0.034	0.245 ± 0.052	0.279 ± 0.103	0.270 ± 0.058	0.175 ± 0.085
	MxD	2.608 ± 0.660	2.676 ± 2.001	3.000 ± 0.000	3.000 ± 0.000	2.873 ± 0.229
	AvSD	0.209 ± 0.059	0.250 ± 0.075	0.243 ± 0.085	0.273 ± 0.053	0.171 ± 0.045
	MxSD	2.745 ± 0.394	2.813 ± 1.924	2.873 ± 0.312	3.281 ± 0.562	2.873 ± 0.229
Thin6C	**AvD**	1.853 ± 0.237	6.523 ± 0.162	1.843 ± 0.266	3.128 ± 0.860	2.801 ± 0.661
	MxD	6.946 ± 1.377	23.293 ± 1.869	7.995 ± 1.052	12.868 ± 1.598	9.749 ± 0.718
	AvSD	1.582 ± 0.188	5.922 ± 0.195	1.897 ± 0.674	2.695 ± 0.805	2.451 ± 0.645
	MxSD	6.946 ± 1.377	23.293 ± 1.869	8.926 ± 1.730	12.868 ± 1.598	9.749 ± 0.718
Thin26C	**AvD**	1.466 ± 0.102	5.523 ± 0.341	1.527 ± 0.187	2.679 ± 0.472	2.610 ± 0.735
	MxD	6.918 ± 1.537	21.807 ± 2.477	7.973 ± 1.256	12.702 ± 1.697	9.519 ± 0.810
	AvSD	1.226 ± 0.124	4.868 ± 0.349	1.222 ± 0.153	2.251 ± 0.450	2.282 ± 0.717
	MxSD	6.918 ± 1.537	21.807 ± 2.477	7.973 ± 1.256	12.702 ± 1.697	9.519 ± 0.810
Thin26CP	**AvD**	0.771 ± 0.110	0.686 ± 0.135	0.755 ± 0.118	0.865 ± 0.150	0.748 ± 0.064
	MxD	2.544 ± 0.797	2.440 ± 0.676	2.864 ± 0.632	7.220 ± 3.239	2.782 ± 0.254
	AvSD	0.664 ± 0.158	0.566 ± 0.184	1.039 ± 0.695	0.961 ± 0.384	0.567 ± 0.048
	MxSD	2.544 ± 0.797	2.676 ± 0.779	5.289 ± 3.291	9.860 ± 3.962	2.782 ± 0.254

4 Application to Abdominal Organs

Our method was applied to sets of manually segmented livers selected from a public database[1] of CT volumes [8]. CT images were acquired with scanners from different manufacturers (4, 16 and 64 detector rows), a pixel spacing between 0.55 and 0.80mm and inter-slice distance from 1 to 3mm. Figure 2 shows medial surfaces for two livers. The extracted medial surfaces show the robustness of our approach. The images in the bottom row show a liver with a remarkably prominent right lobe in its superior aspect, which is captured by our medial representation.

Our next experiment focuses on the representation of multi-organ datasets [14]. Initial results on the medial representation of multiple abdominal organs are shown in Fig. 3. It can be observed that medial representations of neighboring organs contain information about shape and topology that can be exploited for the description of organ shape and configuration.

[1] Collected from sliver07 competition hosted at MICCAI07 and available at sliver07.isi.uu.nl.

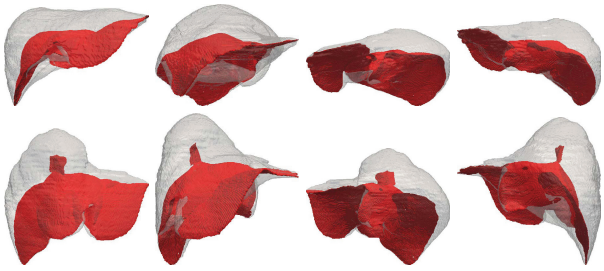

Fig. 2. Medial surfaces from livers. Upper row, normal liver. Bottom, protruding superior lobe.

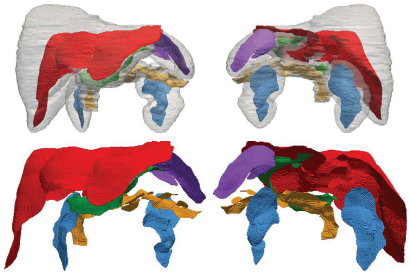

Fig. 3. Abdominal set of organs and surfaces: liver (red), kidneys (blue), pancreas (yellow), spleen (purple), and stomach (green).

5 Conclusions and Discussion

Medial manifolds are powerful descriptors of anatomical shapes. The method presented in this paper overcomes the limitations of existing morphological methods: it extracts medial surfaces without medial axis segments, and the binarization scales well with increasing dimension. Additionally, we have presented a quantitative comparison study to evaluate the performance of medial surface calculation methods and calculate their deviation from an ideal medial surface. Finally, we have shown the performance of our method for the analysis of multiple abdominal organs.

Future work includes the use of the medial surfaces computed using our methods as basis for shape parameterization [20], in order to construct anatomy-based reference systems for implicit registration and localization of pathologies. Further, we will explore correspondences between medial representations of neighboring organs to define inter-organ relations in a more exhaustive way than simply using centroid and pose parameters [10,11,19].

Acknowledgements. This work was supported by the Spanish projects TIN2009-13618, CSD2007-00018, 2009-TEM-00007, PI071188 and NIH Clinical Center Intramural Program. The 2nd author has been supported by the Ramon y Cajal Program.

References

1. Amenta, N., Choi, S., Kolluri, R.: The power crust, unions of balls, and the medial axis transform. Computational Geometry: Theory and Applications 19(2-3), 127–153 (2001)
2. Bigun, J., Granlund, G.H.: Optimal orientation detection of linear symmetry. In: ICCV, pp. 433–438 (1987)
3. Bouix, S., Siddiqi, K.: Divergence-Based Medial Surfaces. In: Vernon, D. (ed.) ECCV 2000. LNCS, vol. 1842, pp. 603–618. Springer, Heidelberg (2000)
4. Bouix, S., Siddiqi, K., Tannenbaum, A.: Flux driven automatic centerline extraction. Med. Imag. Ana. 9(3), 209–221 (2005)
5. Canny, J.: A computational approach to edge detection. IEEE Trans. Pat. Ana. Mach. Intel. 8, 679–698 (1986)
6. Chang, S.: Extracting skeletons from distance maps. Int. J. Comp. Sci. Net. Sec. 7(7) (2007)
7. Haralick, R.: Ridges and valleys on digital images. Comput. Vision Graph. Image Process. 22(10), 28–38 (1983)
8. Heimann, T., van Ginneken, B., Styner, M., Arzhaeva, Y., Aurich, V., et al.: Comparison and evaluation of methods for liver segmentation from CT datasets. IEEE Trans. Med. Imag. 28(8), 1251–1265 (2009)
9. Lee, T.C., Kashyap, R.L., Chu, C.N.: Building skeleton models via 3-D medial surface axis thinning algorithms. Grap. Mod. Imag. Process 56(6), 462–478 (1994)
10. Linguraru, M.G., Pura, J.A., Chowdhury, A.S., Summers, R.M.: Multi-organ Segmentation from Multi-phase Abdominal CT via 4D Graphs Using Enhancement, Shape and Location Optimization. In: Jiang, T., Navab, N., Pluim, J.P.W., Viergever, M.A. (eds.) MICCAI 2010, Part III. LNCS, vol. 6363, pp. 89–96. Springer, Heidelberg (2010)
11. Liu, X., Linguraru, M.G., Yao, J., Summers, R.M.: Organ Pose Distribution Model and an MAP Framework for Automated Abdominal Multi-Organ Localization. In: Liao, H., Edwards, P.J., Pan, X., Fan, Y., Yang, G.-Z. (eds.) MIAR 2010. LNCS, vol. 6326, pp. 393–402. Springer, Heidelberg (2010)
12. Lopez, A., Lumbreras, F., Serrat, J., Villanueva, J.: Evaluation of methods for ridge and valley detection. IEEE Trans. Pat. Ana. Mach. Intel. 21(4), 327–335 (1999)
13. Pudney, C.: Distance-ordered homotopic thinning: A skeletonization algorithm for 3D digital images. Comp. Vis. Imag. Underst. 72(2), 404–413 (1998)
14. Reyes, M., González Ballester, M., Li, Z., Kozic, N., Chin, S., Summers, R., Linguraru, M.: Anatomical variability of organs via principal factor analysis from the construction of an abdominal probabilistic atlas. In: IEEE Int. Symp. Biomed. Imaging, pp. 682–685 (2009)
15. Sabry, H.M., Farag, A.A.: Robust skeletonization using the fast marching method. In: IEEE Int. Conf. on Image Processing, vol. (2), pp. 437–440 (2005)
16. Siddiqi, K., Bouix, S., Tannenbaum, A., Zucker, S.W.: Hamilton-Jacobi skeletons. Int. J. Comp. Vis. 48(3), 215–231 (2002)
17. Styner, M., Lieberman, J.A., Pantazis, D., Gerig, G.: Boundary and medial shape analysis of the hippocampus in schizophrenia. Medical Image Analysis 8(3), 197–203 (2004)
18. Telea, A., van Wijk, J.J.: An augmented fast marching method for computing skeletons and centerlines. In: Symposium on Data Visualisation, VISSYM 2002, pp. 251–259. Eurographics Association (2002)
19. Yao, J., Summers, R.M.: Statistical Location Model for Abdominal Organ Localization. In: Yang, G.-Z., Hawkes, D., Rueckert, D., Noble, A., Taylor, C. (eds.) MICCAI 2009, Part II. LNCS, vol. 5762, pp. 9–17. Springer, Heidelberg (2009)
20. Yushkevich, P., Zhang, H., Gee, J.: Continuous medial representation for anatomical structures. IEEE Trans. Medical Imaging 25(12), 1547–1564 (2006)